Air-Filled SIW Remote Antenna Unit With True Time Delay Optical Beamforming for mmWave-Over-Fiber Systems

Igor Lima de Paula, Laurens Bogaert, Olivier Caytan, *Member, IEEE*, Joris Van Kerrebrouck, Arno Moerman, *Graduate Student Member, IEEE*, Muhammad Muneeb, Quinten Van den Brande, Guy Torfs, *Senior Member, IEEE*, Johan Bauwelinck, *Senior Member, IEEE*, Hendrik Rogier, *Senior Member, IEEE*, Piet Demeester, *Fellow, IEEE*, Günther Roelkens, *Senior Member, IEEE*, and Sam Lemey, *Member, IEEE*

(Invited Paper)

***Abstract*—A low-complexity and efficient mmWave-over-fiber remote antenna unit (RAU) is proposed for broadband transmission and wide-angle squint-free beam steering in the full [26.5–29.5] GHz n257 5G band. It leverages an optical beamforming network (OBFN), implemented on a silicon photonics integrated circuit, and a broadband optically enabled 1x4 uniform linear array (ULA). The antenna elements (AEs) of the ULA are implemented in air-filled substrate-integrated-waveguide technology. They adopt an improved aperture-coupled feeding scheme to achieve high efficiency, high isolation and minimal back radiation over a broad frequency band. Each AE is compactly integrated and co-optimized with a dedicated opto-electrical transmit chain, maximizing the RAU's performance, including beamforming flexibility and energy efficiency, while minimizing its size. The separately packaged OBFN implements true-time-delay beamforming by means of four switchable optical delay lines that are capable of discretely tuning the delay difference between AEs with a resolution of 1.6 ps, up to a maximum delay of 49.6 ps to fully exploit the ULA's full grating-lobe-free scan range. The measured AEs are excellently matched in the [25.1–30.75] GHz band, exhibit high isolation (>15 dB) in the operating band, and feature a stable peak gain of 6.8 ± 0.72 dBi with a beamwidth of at least 95°. Additionally, optical beamforming was successfully demonstrated by steering the RAU's beam towards angles up to 51.8° without grating lobes. The optically enabled 1 × 4 ULA successfully establishes a 64-QAM wireless communication link at 2.2 Gbaud (13.2 Gbps) while beam steering up to 50° with an error vector magnitude below 7.6%.**

***Index Terms*—Analog radio-over-fiber, antenna arrays, distributed antenna systems, microwave photonics, optical beamforming networks, true time delay.**

Manuscript received 31 March 2022; revised 22 June 2022; accepted 24 June 2022. Date of publication 30 June 2022; date of current version 21 October 2022. This work was supported in part by Ghent University under Grant BOF14/GOA/034, in part by the Methusalem funding of the Flemish Government under Grant Smart Photonic Chips and under Grant SHAPE: Next Generation Wireless Networks, and in part by the European Research Council through ATTO: A new concept for ultrahigh capacity wireless networks under Grant 695495. *(Igor Lima de Paula and Laurens Bogaert contributed equally to this work.) (Corresponding author: Igor Lima de Paula.)*

Igor Lima de Paula, Olivier Caytan, Joris Van Kerrebrouck, Arno Moerman, Quinten Van den Brande, Guy Torfs, Johan Bauwelinck, Hendrik Rogier, Piet Demeester, and Sam Lemey are with the IDLab, Department of Information Technology, Ghent University-imec, 9052 Ghent, Belgium (e-mail: igor.limadepaula@ugent.be; olivier.caytan@ugent.be; joris.vankerrebrouck@ugent.be; arno.moerman@ugent.be; quinten.vandenbrande@ugent.be; guy.torfs@ugent.be; johan.bauwelinck@ugent.be; hendrik.rogier@ugent.be; piet.demeester@ugent.be; sam.lemey@ugent.be).

Laurens Bogaert, Muhammad Muneeb, and Günther Roelkens are with the Photonics Research Group, Department of Information Technology, Ghent University-imec, 9052 Ghent, Belgium (e-mail: laurens.bogaert@ugent.be; muhammad.muneeb@ugent.be; gunther.roelkens@ugent.be).

Color versions of one or more figures in this article are available at https://doi.org/10.1109/JLT.2022.3187555.

Digital Object Identifier 10.1109/JLT.2022.3187555

I. Introduction

THE mmWave frequency band will play a vital role in the (beyond) 5G era to address the ever-increasing demands of emerging wireless applications and to enable the Internet of Everything (IoE), offering unprecedented wireless data rates (up to multi-Gbps per user and up to one Tbps aggregated), ultra-low-latency ($<100\,\mu$s) and ultra-reliability (99.99999%) to a massive number of end users [1], [2]. While this shift to higher frequencies provides the required bandwidth, it is accompanied with challenging propagation conditions [3]. Fortunately, the short wavelengths enable compact implementation of large antenna arrays. The increased path loss and high mobility of users can then be efficiently countered through adaptive beamforming, while (massive) MIMO techniques can be leveraged to further optimize throughput/spectral efficiency [4]. Still, a conventional co-located approach, in which all antennas are grouped in the same aperture, is prone to line-of-sight (LoS) blockage and therefore insufficient to maintain high data rates in challenging real-life scenarios with frequent non-LoS (NLoS) conditions, as required by next-generation IoE applications, such as holographic telepresence, cyber-physical systems in Industry 4.0 and immersive augmented and virtual reality [2].

To improve link reliability in case of NLoS conditions, current-generation solutions either revert to sub-6 GHz frequencies or leverage advanced beamforming algorithms to exploit reflections in the environment, thereby compromising on link capacity and/or quality. Recently, [5] launched the innovative concept of a large intelligent surface (LIS) to provide reliable, high-data-rate wireless communication. This is a large

contiguous surface of electromagnetic radiators surrounding the user equipments (UEs), placing the UEs in the LIS's near field. This enables holographic beamforming in which energy can be focused in three dimensions. Another interesting approach concerns the use of intelligent reflective surfaces (IRSs) [6]. While both concepts offer great potential, much more research is required to practically implement these in the mmWave band [7]. Furthermore, in [8], mmWave-over-Fiber distributed antenna systems (DASs) are advocated to provide high throughput and reliable coverage in harsh and challenging real-life environments. In such an architecture, the core functionality is centralized in a central office (CO) and optical fiber is used to efficiently distribute the broadband mmWave signals to multiple remote antenna units (RAUs) that are strategically distributed in the UEs' environment. As the mmWave signal modulated on the optical carrier is already at the correct frequency in a mmWave-over-fiber scheme, two advantages arise over other fiber distribution schemes, paving the way for the practical realization of the aforementioned LIS concept [8], [9] and for next-generation small-cell-based radio-access networks (RANs) [10], [11]. First of all, tight synchronization among all distributed RAUs can be guaranteed. Second, it allows for low-complexity laser-free RAUs [12], which only need to implement opto-electrical conversion (and vice versa) and amplification of the mmWave signal and to radiate/receive through a (multi-)antenna system. In the context of a mmWave-over-fiber link, two major architectural trade-offs need to be made for the beamformer, having a significant impact on system performance and cost. First, the beamforming network should either be deployed at the CO or at the RAUs. While the former leads to a higher degree of centralization, this significantly increases the amount of traffic between the CO and RAU, depending on the number of antenna elements. Second, the implementation domain must be selected to be either optical or electrical. Optical beamforming techniques can implement both phase shifts and true time delays (TTDs) and offer compelling advantages over an electrical approach, such as wide bandwidths, low losses and immunity to electromagnetic interference (EMI) [13].

This work proposes a novel, efficient mmWave RAU that implements broadband transmission and wide-angle, squint-free beam steering in the full [26.5–29.5] GHz n257 5G band by leveraging an in-house developed optical beamforming network (OBFN) on a photonic integrated circuit (PIC) and a dedicated 1×4 uniform linear array (ULA). Its antenna elements (AEs) are based on the air-filled substrate-integrated-waveguide (AFSIW) technology to guarantee broadband and efficient operation, and to obtain low mutual coupling between the AEs, enabling grating-lobe-free beam steering over a range of $100\,^{\circ}$. Each AE is compactly integrated and co-optimized with a dedicated opto-electrical transmit chain [12], maximizing performance, including beamforming flexibility and energy efficiency, while minimizing its size and weight. The separately packaged OBFN is implemented on imec's passive silicon photonics platform and contains four switchable optical delay lines (SODLs), supporting the ULA's full grating-lobe-free scan range without beam squint by means of TTD beamforming [14].

This paper is an invited extension of our work presented at the International Topical Meeting on Microwave Photonics [15], including a more detailed description of the antenna array and the opto-electrical transmit chain, focusing in particular on their compact integration, the adopted co-design strategy and the assembly of the entire unit. The proposed RAU is also validated more extensively by demonstrating optical beam steering towards angles up to $50\,^{\circ}$, and by describing several multi-Gbps fiber-wireless communication experiments. To the best of the authors' knowledge, this is the first time that a mmWave-over-Fiber RAU with custom-tailored OBFN PIC has been proposed, whose beam steering performance and power efficiency are maximized by compact integration and co-optimization of an opto-electrical transmit chain with an AFSIW-based antenna array.

The remainder of this paper is organized as follows. Section II provides an overview of the proposed system architecture. Next, the OBFN and the optically enabled antenna array are extensively discussed in Sections III and IV, respectively, while the measurement results are presented in Section V. Subsequently, Section VI conducts an in-depth comparison with the state-of-the-art and explores possible future research paths. Section VII concludes this paper.

II. System Architecture

Fig. 1 depicts a mmWave-over-fiber DAS deployed in a challenging indoor environment to provide reliable high-data-rate coverage to the UE, even in the presence of multiple obstacles. In this approach, RAUs are strategically distributed and integrated in the UE's environment to provide at least one line-of-sight path, whereas the CO distributes the mmWave signals over fibers towards the different RAUs. By generating the mmWave signals at the CO and directly modulating them onto an optical carrier, the most expensive and power-consuming hardware is centralized at the CO. The advantages of optical fiber are leveraged to efficiently distribute mmWave signals with excellent interference immunity, while guaranteeing tight synchronization between RAUs [8]. In addition, it leads to low-complexity/low-power RAUs as power-hungry mixers and analog-to-digital/digital-to-analog converters (ADC/DACs) are eliminated at the RAU. In fact, they only need to implement opto-electrical conversion, amplification, and potentially beamforming. The latter is detailed in the inset of Fig. 1, depicting the architecture of the proposed mmWave-over-Fiber RAU. It is designed for broadband downlink transmission and wide-angle squint-free beam steering in the complete [26.5–29.5] GHz n257 5G band. It consists of an in-house developed true-time-delay OBFN implemented on a silicon PIC (Section III) and an optically enabled antenna array (Section IV). The latter comprises four highly efficient printed-circuit-board (PCB)-based AFSIW AEs, each compactly integrated with a dedicated photoreceiver (including an electro-optical transducer and a low-noise amplifier (LNA)), arranged in a 1×4 ULA configuration. The RAU's 1×4 antenna array, whose elements are excited by independent photoreceivers, is capable of performing adaptive beamforming to focus the radiated power in the UE's direction, thus countering the large free-space path loss, a major hurdle at mmWave. By integrating the OBFN at the RAU, the data stream can be transported to the RAU via a single optical fiber, while the beamforming is entirely executed by the RAU.

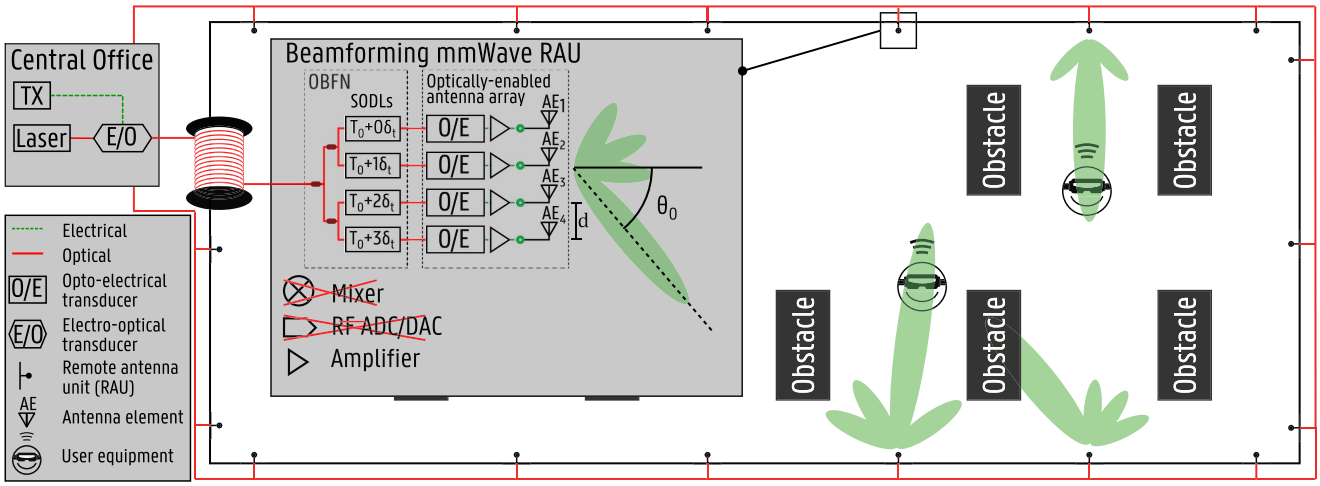

Fig. 1. System architecture of a mmWave-over-fiber distributed antenna system (DAS) to provide robust and high-data-rate coverage in challenging indoor environments. The inset depicts the proposed downlink mmWave-over-fiber remote antenna unit (RAU), consisting of an in-house developed optical beamforming network (OBFN) and a dedicated broadband optically enabled antenna array. ADC: analog-to-digital converter; DAC: digital-to-analog converter; SODL: switchable optical delay line.

III. Optical Beamforming Network

The OBFN is designed to perform broadband beam steering with a 1×4 uniform linear mmWave antenna array. Therefore, it equally splits the modulated optical signal, transmitted by the CO, over the four antenna elements of the RAU, while applying the appropriate beamforming coefficients, as shown in the inset of Fig. 1. The OBFN should offer low insertion loss, low insertion loss variation for all beamforming settings, low power consumption and it should accurately implement the expected beamforming coefficients. Additionally, this building block should provide a constant group delay. This is essential to achieve broadband beamforming without beam squint [14], which would yield an undesired beam direction offset as a function of frequency.

To fulfill the constant group delay requirement, the beamforming coefficients are implemented by reconfigurable optical delay lines between the outputs of the power splitter and the AEs. This technique, in which the time delay for every AE is adjusted, is known as TTD and offers broadband squint-free beam steering [14]. A compact optical-domain TTD device is implemented in the proposed OBFN by SODLs [16], [17] (inset of Fig. 1). By switching between shorter or longer optical path lengths, as shown in Fig. 2(a), this strategy enables discrete delay tuning with a tuning resolution of ΔT and a tuning range of $(2^{\mathrm{N}} - 1) \times \Delta\mathrm{T}$, with N the total number of bits. The time-delay difference between consecutive antenna elements (δ_t) and the inter-antenna-element spacing d determine the steering angle θ_0, according to [14]

$$\sin(\theta_0) = \frac{c\delta_t}{d}, \tag{1}$$

showing that the steering angle (θ_0) is only determined by the delay difference between adjacent elements and not by the absolute delay of each separate AE. Hence, the offset delay T_0 does not play a role as long as each SODL in the OBFN has the same T_0.

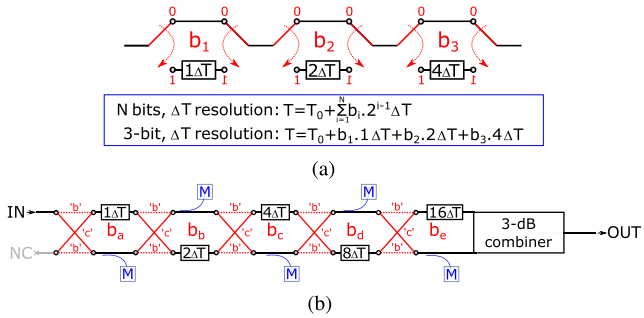

Fig. 2. Conceptual representation of an SODL: (a) Standard 3-bit SODL. (b) Adopted 5-bit SODL to reduce number of control voltages. M: power monitor port; NC: not connected, 'b': bar state, 'c': cross state.

Our four-channel OBFN is implemented in a silicon photonics platform to benefit from its high index contrast that permits small bend radii with minimal loss, yielding compact, low-loss delay lines. The switches, realized by thermally tunable Mach-Zehnder interferometers (MZIs), are compact and generate low switching loss, at switching speeds in the order of 10 μs. In the proposed OBFN, an improved version of the standard SODL was applied [Fig. 2(b)]. In the standard SODL [Fig. 2(a)], two switches are used per bit: One switch at the input of every bit selects either the short or long optical path for that specific SODL section, while another switch at the output of every bit recombines both paths without excessive loss. The improved architecture [16], [17] [Fig. 2(b)] only requires a single dual-input, dual-output switch per bit, thereby halving the required number of control voltages. However, in this architecture, preceding bits will determine at which switch's input port the light will be present. Consequently, the correct switch setting ('bar' ('b') or 'cross' ('c') state) not only depends on the required delay for the current bit, but also on all the preceding bits. At the output, we used a 3-dB power combiner instead

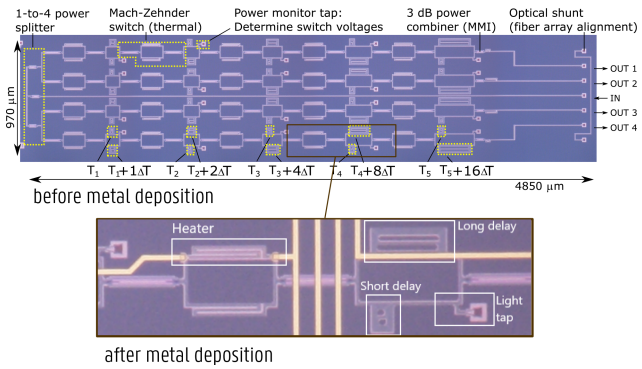

Fig. 3. Microscope image with layout view of the passive Si-Photonics chip. Inset: 1 bit of the SODL, a structure that selects between a long or a short optical waveguide through a thermally controlled Mach-Zehnder interferometer (MZI), switch. MMI: multi-mode interferometer.

of a final switch. Even though this combiner adds an inherent 3-dB insertion loss, it minimizes the number of control signals needed to correctly set the delay setting and the associated power consumption. Additionally, to execute post-fabrication calibration of the switch states, each short path of the adopted SODL includes a directional coupler, tapping 2.5% of the light, as indicated in Fig. 2(b).

In particular, imec's passive silicon photonics platform is leveraged to implement the proposed OBFN. It features a silicon-on-insulator (SOI) stack with a functional Si layer that is 220-nm thick and accommodates both rib and strip waveguides. We employed the standard C-band strip waveguides with a height of 220 nm and a width of 450 nm for the fabricated OBFN. These waveguides have a loss of 1.3 dB/cm, a group index of 4.26 at 1550 nm and bend losses limited to 0.009 dB per 90° bend for a 5 μm bend radius. Both the reference path and the long path waveguides have 18 bends, and the power taps are judiciously placed in the short path to minimize insertion loss variations through all switch states. Based on the group index, this C-band waveguide yields approximately 1 ps delay per 70 μm. An annotated microscope image of the fabricated passive Si-Photonics chip is shown in Fig. 3. This design is optimized for a 1×4 uniform linear antenna array and contains four delay lines with 5-bit discrete tunability and a delay resolution of $\Delta T = 1.6$ ps, corresponding to a maximum delay of 49.6 ps and a maximum delay sequence given by {0 ps, 16 ps, 32 ps, 48 ps}. This yields a scan angle of $\theta_{0,\max} = 63.6°$ at an AE spacing of $d = 5.36$ mm, i.e., half the wavelength at 28 GHz, being the center operating frequency of the RAU. The total chip area equals 4.7 mm^2 and the optical I/O of the OBFN is achieved by using a grating coupler array. Two metal layers were added during post-processing of the SOI chip shown in Fig. 3. First, a heater layer (150 nm Ti + 15 nm Au) was added to enable thermal tuning of the MZI. Second, metal routing and bondpads were added in an additional layer (40 nm Ti + 800 nm Au). The deposited heaters are approximately 500 μm long and 2 μm wide, yielding resistances of about 1050 Ω. The inset of Fig. 3 displays a microscope image of the circuit for a single bit, after metallization. Afterwards, an OBFN assembly was constructed by bonding the photonic chip to a PCB (see inset of Fig. 12), such that the switch bondpads could be wirebonded to the PCB tracks and such that they are easily accessed by a pin header. Finally, a fiber array was attached to the I/O grating couplers.

IV. AFSIW Remote Antenna Unit

A. Antenna Array Topology

The proposed mmWave antenna array is designed for highly efficient operation and grating-lobe-free beam steering from $\theta_0 = -50°$ to $\theta_0 = 50°$ in the [26.5–29.5] GHz n257 5G band, thereby providing the RAU with broadband and wide-angle beam steering. Therefore, the magnitude of the reflection coefficient $|S_{11}|$ of each AE should be lower than -10 dB and the mutual coupling between the AEs must be limited to -15 dB in the entire frequency band. Furthermore, the AE footprint should be sufficiently small to prevent grating lobes, which are undesired alias main beams [18] that may appear in the radiation pattern. In particular, to ensure the main beam can be steered up to $\pm\theta_{0,\max} = 50°$ without introducing grating lobes, the spacing d between the antenna elements, compared to the free-space wavelength λ_2 at 29.5 GHz, must be limited to [19]

$$d < \frac{\lambda_2}{1 + \sin|\theta_{0,\max}|} = 5.76\,\text{mm}. \tag{2}$$

Additionally, the AE's total efficiency is targeted to be higher than 85% to minimize both the reflection loss at the antenna interface and the internal antenna losses, thereby minimizing energy waste and maximizing the range of the RAU. Moreover, the antenna array should also facilitate integration of the opto-electronic RAU components on its feedplane directly behind the AEs to minimize interconnect losses and to reduce the overall system footprint.

The proposed RAU's antenna array, depicted in Fig. 4(b), fulfills all aforementioned specifications by adopting an AFSIW cavity-backed patch antenna topology. As demonstrated in [20], such a topology achieves high efficiency, wide impedance bandwidth in a compact footprint, and it minimizes mutual coupling, even when the AEs are closely packed. The antenna array consists of three inexpensive dual-layer PCBs manufactured through standard PCB processing technology, being PCB_1 (0.254-mm Rogers 4350B), implementing the radiating patch; PCB_2 (1-mm FR4), incorporating an AFSIW cavity by locally removing the lossy substrate material and subsequent metal plating the created inner walls; and PCB_3 (0.254-mm Rogers 4350B), where the antenna feed is deployed. The air-filled metallized cavity in PCB_2 lowers the Q-factor of the antenna, enabling broadband operation. It also avoids penetration of the electromagnetic fields in the lossy substrate, yielding high radiation efficiency and large isolation in compact antenna arrays. These benefits of AFSIW are showcased in [20], demonstrating a measured total efficiency of at least 85% over a frequency band as wide as 26.8%, and in [21], comparing the air-filled and dielectric-filled versions of a cavity-backed antenna. Although AFSIW-based components are typically larger than their dielectric-filled counterparts due to the larger wavelength observed in the air [21], the proposed antenna element is miniaturized by exploiting the capacitive

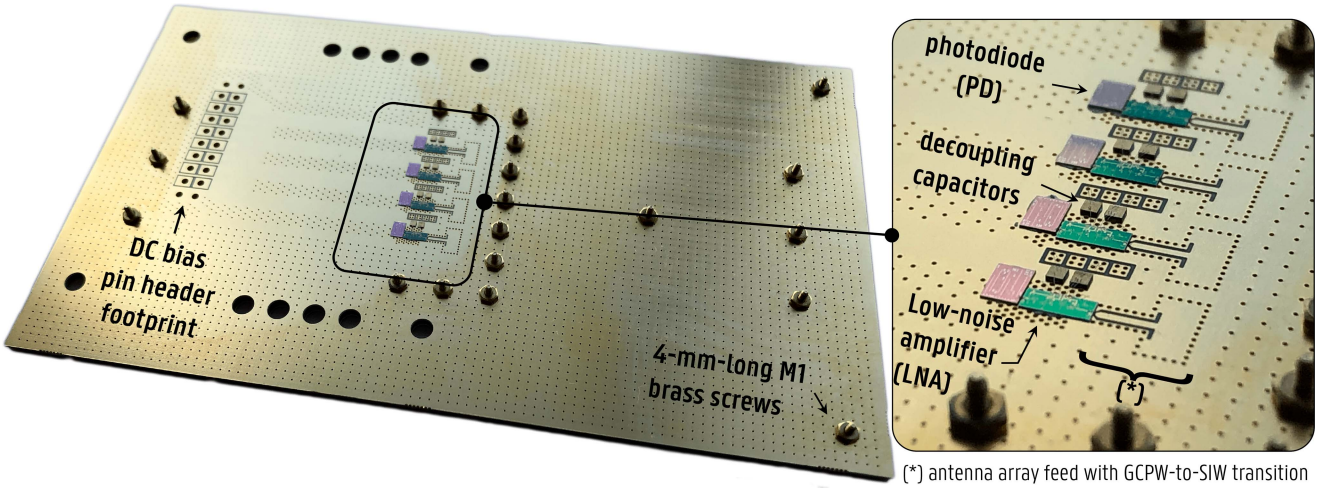

(a) Optically enabled antenna array after photoreceiver integration

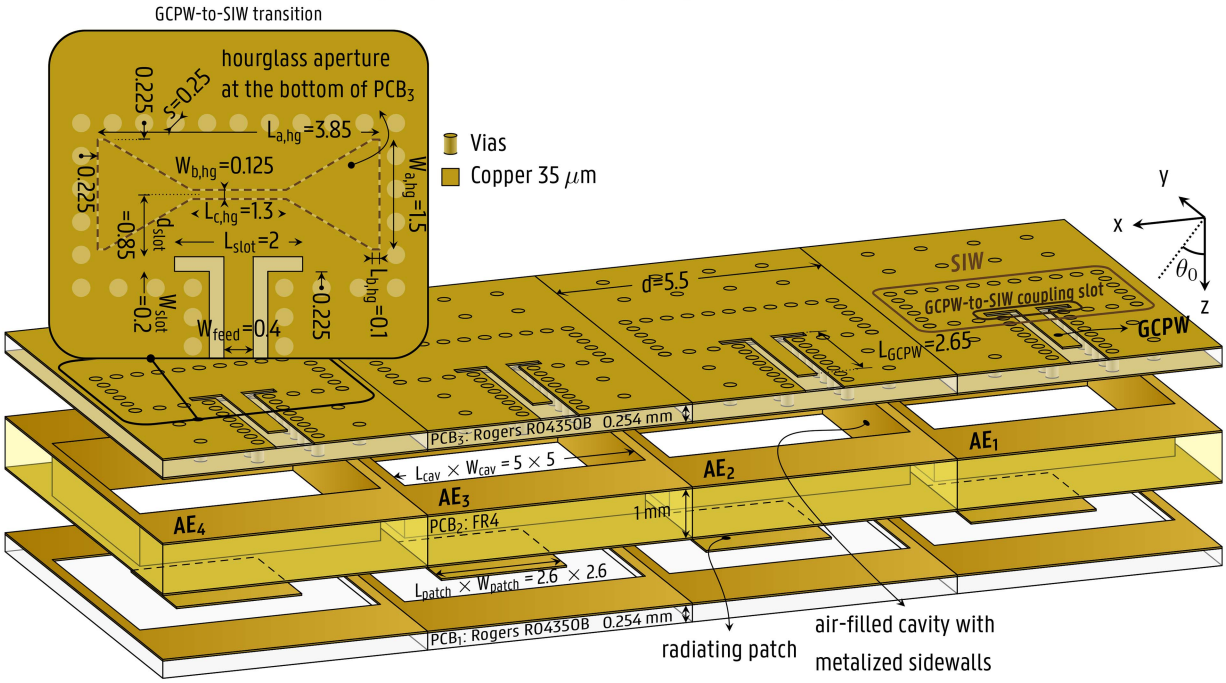

(b) RAU's Antenna array

Fig. 4. Optically enabled air-filled substrate-integrated-waveguide (AFSIW) antenna array. (a) Prototype before being assembled with optical fiber pigtails. (b) Exploded view of the RAU's antenna array consisting of printed circuit boards (PCBs) i.e., PCB_1 (RO4350B), PCB_2 (FR4) and PCB_3 (RO4350B). Inset at the left: antenna feedplane dimensions in millimeters.

loading effect of the metallized air cavity on the patch, achieving an antenna footprint of $\mathrm{W_{cav}} = 5$ mm by $\mathrm{L_{cav}} = 5$ mm [20]. Furthermore, compared to the antenna introduced in [20], the proposed antenna's feed plane has been improved to minimize back radiation originating from the aperture-coupled feed. This is essential to provide sufficient isolation between the active electronic components of the RAU and the electromagnetic waves radiated by the AEs. It requires a clear separation between the antenna feed plane, where the components are mounted, and the radiating aperture at the opposite side. In addition, low back radiation is also of major importance to achieve a high antenna-to-integration platform isolation [22] and, hence, to maintain high antenna performance in real-life conditions where the platform on which the RAU will be installed is not a priori known. Thereto, a dedicated grounded-coplanar-waveguide-to-substrate-integrated-waveguide (GCPW-to-SIW) transition [see inset of Fig. 4(b)] is combined with an hourglass-based aperture-coupling feed to efficiently excite the antenna with minimal back radiation, while enabling compact integration of active electronics. The GCPW transmission line enables direct interconnection to the LNA output. A downlink signal, originating from the LNA, excites the quasi-TEM mode in the GCPW section, after which the GCPW-to-SIW-transition converts this mode to a TE_{10} mode in the short SIW section. The fields in this SIW section excite the AFSIW cavity in PCB_2 via the hourglass-shaped coupling-aperture at the bottom of PCB_3.

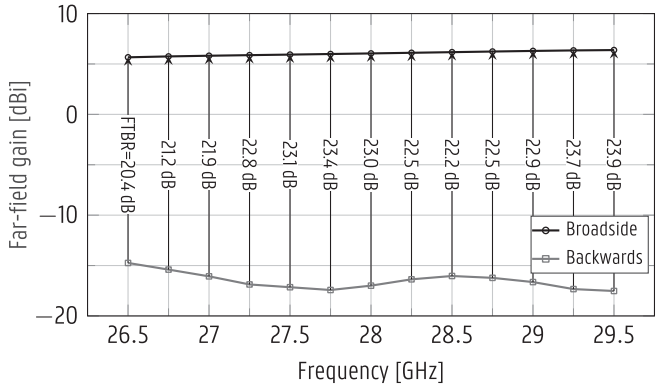

Fig. 5. Simulated broadside and backwards far-field gain and corresponding front-to-back ratio of an inner antenna array element AE_2.

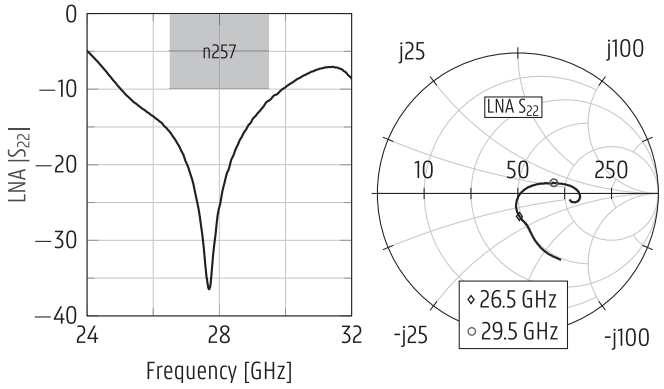

(a) (b)

Fig. 6. Measured low-noise amplifier (LNA) output reflection coefficient: (a) Magnitude. (b) Smith chart.

The GCPW-to-SIW transition [23] is based on a coupling slot positioned at the junction between both waveguide technologies [Fig. 4(b)]. Because the slot length, $\mathrm{L_{slot}}$, is substantially smaller than $\lambda_2/2$ and the GCPW is not open-ended, the antenna feed will not introduce considerable back radiation, as will be shown in the sequel. Moreover, the proposed AE enables broadband impedance matching to a wide variety of source impedances by tuning the hourglass aperture, the cavity and the patch parameters [20], as well as the GCPW-to-SIW transition parameters, $\mathrm{L_{slot}}$, $\mathrm{d_{slot}}$ and $\mathrm{W_{slot}}$.

Fig. 5 shows the broadside antenna gain (antenna gain along the +z-direction), the backward antenna gain (antenna gain along the -z-direction) and the front-to-back ratio (FTBR, defined as the ratio of the broadside and backward antenna gain). The novel antenna feed guarantees a FTBR of at least 20.4 dB. This is in contrast to the topology introduced in [20], whose FTBR is only 7.9 dB in the [26.5–29.5] GHz band.

Based on the proposed AE, a 1×4 ULA can then be realized that allows beam steering towards any direction in the xz-plane, such that the scan angle θ_0, defined in Fig. 4, varies within the interval [-50°, 50°].

B. Optically Enabled Antenna Array

To build the optically enabled RAU, the antenna array was further optimized to enable compact integration of four in-house developed optical photoreceivers [12], [24], comprising a silicon waveguide coupled Ge-on-Si photodiode (PD), a GaAs LNA and decoupling chip capacitors. The LNA, described in detail in [24], delivers a maximum gain of 24 dB, over a 3-dB bandwidth in the range [23.5–31.5] GHz, while exhibiting a low noise figure of 2.1 dB. Its output-referred third-order intercept point (OIP3) equals 26.5 dBm at a power consumption of 303 mW. The output impedance of the adopted LNA is shown in Fig. 6. Although the LNA output was designed to match to 50 Ω [24], its impedance is frequency dependent and will deviate from the targeted 50 Ω.

Therefore, two different optimization strategies for the antenna array are considered, resulting in slightly different dimensions for the features of the feed PCB ($\mathrm{PCB_3}$). The first strategy adopts a conventional approach in which the input impedance of all AEs are matched to a standard 50-Ω impedance. In contrast, the second strategy conjugately matches the AEs' input impedance to the LNAs' output impedance over the entire operating frequency band, leading to a co-optimized design with maximal power transfer from the LNAs to the AEs. In both strategies, the inter-element spacing d was chosen to be 5.5 mm (i.e. 0.54 λ_2 at 29.5 GHz) as shown in Fig. 4, as a compromise to decrease mutual coupling between the AEs, while allowing for a theoretical maximum grating-lobe-free scan range up to $\theta_0 = \pm 58°$, fulfilling the interelement-spacing criterion expressed by (2).

To compare performance between both strategies, the simulated active reflection coefficient magnitude $|\Gamma_2^a|$ is displayed in Fig. 7 for the second array element [see Fig. 4(b)], considering both antenna array optimizations and different scan angles. The active reflection coefficient of the m$^{\text{th}}$ AE, $|\Gamma_m^a|$, defined in [25], is the ratio between the reflected power and the incident power of the m$^{\text{th}}$ AE when all the other AEs are also excited. Therefore, the active reflection coefficient depends not only on the m$^{\text{th}}$ AE's reflection coeffient, but also on the mutual coupling between the m$^{\text{th}}$ AE and the other antenna elements and their respective excitations. Hence, since the excitation phases of the AEs are a function of the scan angle, the $|\Gamma_m^a|$ also depends on the scan angle. Remark that both in Fig. 7(a) and (b), $|\Gamma_2^a|$ is referenced to the conjugate LNA's output impedance to indicate the power transfer between the AEs and the LNAs. In particular, it can be seen that the $|\Gamma_2^a|$ of the co-optimized antenna array remains below -9.3 dB, such that this design will accept at least 88% of the input power for all considered scan angles, while for the conventional 50-Ω version, the $|\Gamma_2^a|$ increases to -6.5 dB for a scan angle of $\theta_0 = 50°$ meaning that only 78% of the power is accepted. Similar behavior can be seen for the other AEs in the antenna array. Hence, even in this worst-case scenario, where the LNA was designed to be matched to 50 Ω, the co-optimization strategy leads to a significantly higher power transfer from LNAs to AEs, thereby enabling a broader beam steering range and a total efficiency above 85% for all scan angles between [$-50°$, 50°]. Moreover, the advantages of co-optimization will become even more pronounced when the preceding active electronics

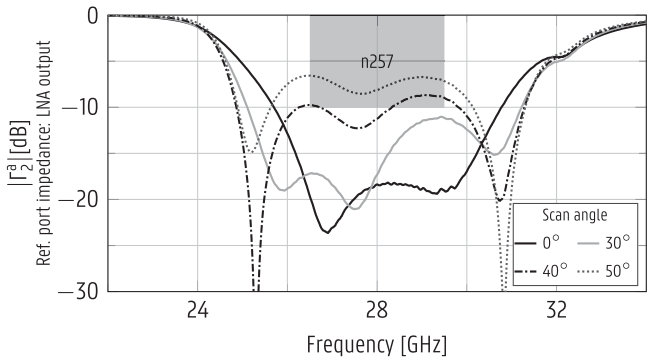

(a) Strategy 1: Optimized for 50-Ω port impedance

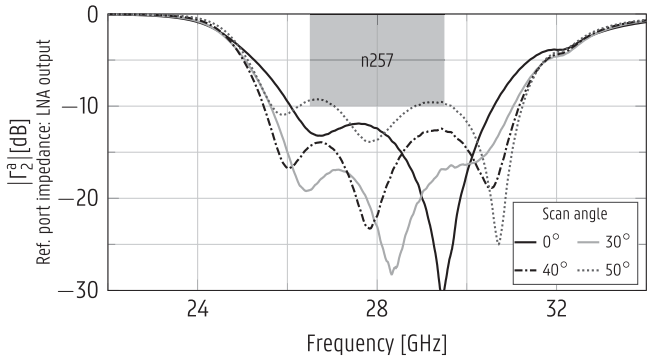

(b) Strategy 2: Optimized for LNA output port impedance

Fig. 7. Simulated magnitude of the active reflection coefficients of element 2 of both versions of the antenna array, when steering the beam to $\theta_0 = 0°$, 30°, 40° and 50°. The reflection coefficients are referred to the conjugated LNA output impedance.

deviate more from the 50-Ω standard [26]. In future designs, this approach can be used to omit the LNA's output impedance matching network, thereby eliminating its inherent loss and resulting in a broader bandwidth in a compact overall footprint [27].

C. Prototype Fabrication

Both antenna arrays were optimized by means of CST Microwave Studio's frequency domain solver. The final dimensions of the 50-Ω antenna array are annotated in Fig. 4, while for the antenna array conjugately matched to the LNA's output impedance, the dimensions were modified to $L_{slot} = 2.2$ mm, $W_{a,hg} = 0.75$ mm, $W_{b,hg} = 0.15$ mm, $d_{slot} = 0.9$ mm and $L_{GCPW} = 2.6$ mm. As a proof of concept, the dual-layer PCBs composing the 1×4 antenna array that serves as an integration platform for the four optical photoreceivers were fabricated at Eurocircuits [28] by using standard PCB manufacturing technology. Next, the PCBs were aligned and screwed together with 4-mm-long M1 brass screws. In addition to this prototype, hereafter referred to as RAU-AA and depicted in Fig. 4, a stand-alone antenna array (hereafter called SA-AA) was fabricated, where each AE is interconnected to end-launch connectors by extended GCPW tracks, so that the antenna array elements could be individually characterized.

In the final step, the components of the photoreceiver were assembled in our cleanroom by means of a pick-and-place tool and

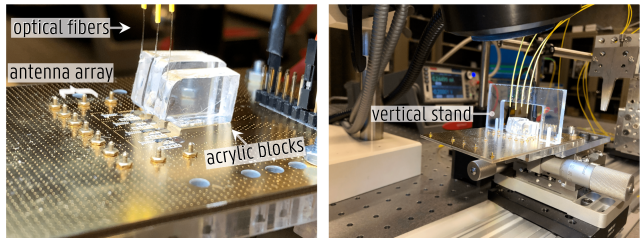

(a) Gluing fibers to PD grating coupler (b) Gluing fibers to vertical stand

Fig. 8. Assembling single-mode optical fibers to the optically enabled prototype by (a) accurate positioning and gluing the fiber core to the photodiode (PD) grating coupler and (b) gluing the fibers to an acrylic vertical stand.

the electrical interconnections between the chips and the antenna feeds were established by bondwires made of aluminum, with a diameter of 25 μm [Fig. 4(a)]. Afterwards, single-mode optical fibers were vertically coupled to the PD's grating coupler, as illustrated in Fig. 8, by accurately situating the flat-cleaved fibers via a manual XYZ positioner, while searching for the position and landing angle that lead to the maximum PD photocurrent. At this position and at an angle of 12° with the normal, the fiber was glued with ultraviolet-curing epoxy to the PD grating coupler. Additionally, the fibers were glued to an acrylic block, enforcing the correct landing angle, and to a vertical stand for extra support.

Remark that the assembly with fiber vertical coupling is needed for the measurements described in Section V. Section VI will describe future steps to omit this complex and time-consuming step.

V. Results

A. Antenna Array

To validate the passive antenna array, the four-port S-parameters of the SA-AA prototype were measured with an Agilent E8364B vector network analyzer (VNA).

The GCPW track of each AE feed was extended to connect through a solder-free V-type (1.85 mm) Southwest Microwave end-launch connector, which was de-embedded by Thru, Reflect, Line (TRL) calibration, such that the port plane is positioned as indicated by L_{GCPW} in Fig. 4(b). The measured and simulated magnitude of the S-parameters are displayed in Fig. 9, exhibiting excellent agreement. Fig. 9(a) shows that the antenna array fulfills the reflection coefficient $|S_{11}| < -10$ dB requirement in the [25.0–30.95] GHz and [25.1–30.75] GHz frequency band for AE_1 and AE_2, respectively. In the [26.5–29.5] GHz 5G n257 band, the $|S_{11}|$ remains below -16.6 dB. Furthermore, the measured magnitudes of the mutual coupling coefficients [Fig. 9(b)] remain lower than -15 dB in the operating band, proving an inter-antenna isolation above 15 dB. The coupling is the highest between adjacent AEs, but quickly decreases as the AEs are spaced further apart.

The far-field embedded radiation patterns of the antenna array were measured in our anechoic chamber equipped with an NSI-MI spherical antenna measurement system and a Keysight

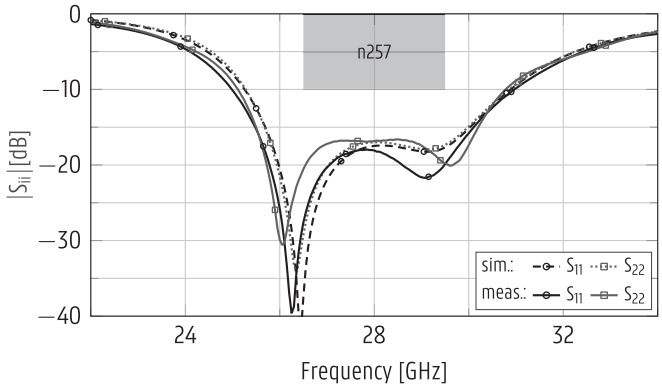

(a) Reflection coefficients

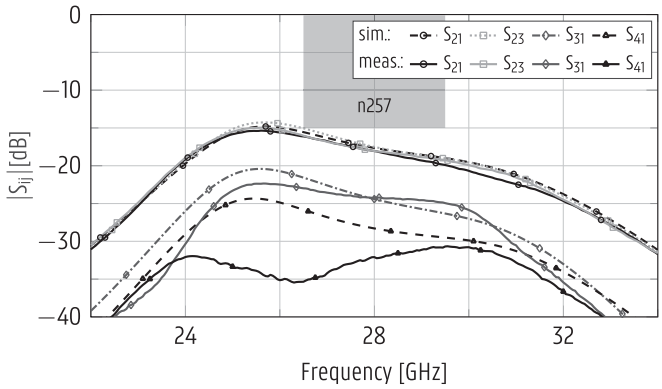

(b) Mutual coupling coefficients

Fig. 9. Simulated and measured magnitude of the S-parameters of the 1 × 4 antenna array (SA-AA) referred to 50 Ω.

N5242 A PNA-X VNA. The gains were calibrated through gain comparison with a WR-34 standard gain horn. The embedded radiation patterns are those obtained for each AE of an antenna array with all other AEs terminated by 50 Ω. Fig. 10 displays the simulated and measured embedded radiation patterns for AE 2 at the center and edge frequencies of the n257 5G band, showing again a good agreement. In the [26.5–29.5] GHz band, AE_2 exhibits a stable peak gain, lying within 6.8 ± 0.72 dBi, and a half power beamwidth (HPBW) in the xz-plane of at least 95°.

B. Optical Beamforming Network

Next, the proposed OBFN, consisting of four SODLs, is characterized. First, a calibration measurement was carried out to determine the required switch voltages for all SODL states at room temperature (25° C) and for a wavelength of 1550 nm. Based on these measurements, it was found that the maximum voltage level needed for all switches was 5.9 V. In addition, the average required power per channel was 82.5 mW, corresponding to 16.5 mW per switch. Taking into account that 20 control voltages are needed to set the 4-channel OBFN, the total average power consumption equals 330 mW.

Afterwards, the delay times produced for each setting of the SODL were measured by the setup depicted in Fig. 11(a). In this setup, a Mach-Zehnder modulator (MZM, Fujitsu FTM7937EZ biased at quadrature point) modulates a 28 GHz sine wave on

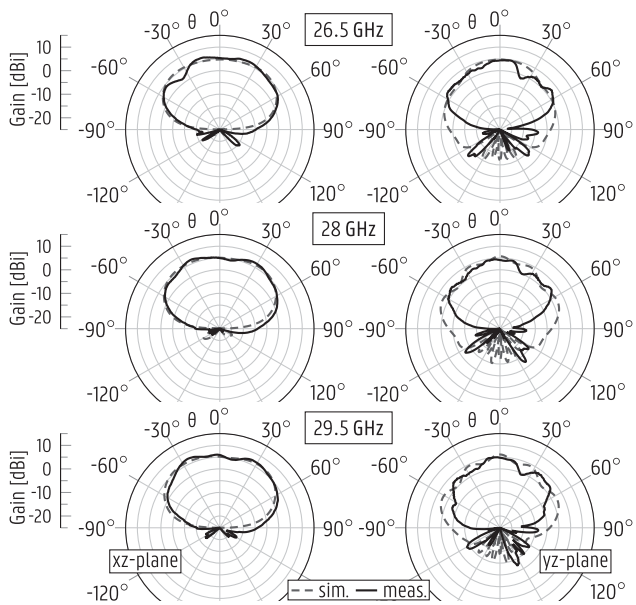

Fig. 10. Simulated and measured radiation pattern of the center element of the 1 × 4 antenna array (SA-AA).

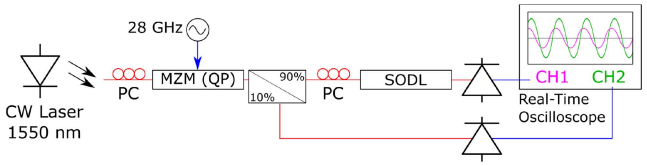

(a)

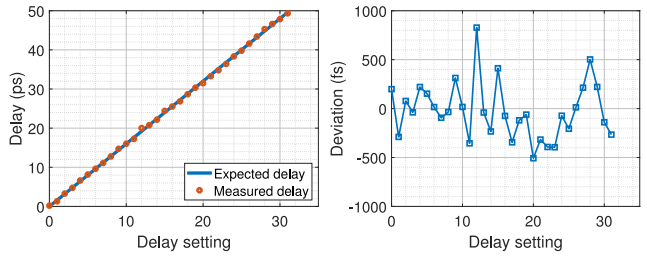

(b)

Fig. 11. Time delay performance of the proposed SODL. (a) Measurement setup (CW: continuous wave; MZM: Mach Zehnder Modulator; QP: Quadrature Point; PC: Polarization Controller). (b) Measured versus expected time delay and their corresponding deviation.

a continuous-wave (CW) 1550-nm optical carrier. The resulting optical signal was split up into a reference path, tapping 10% of the power and a main path, passing through the SODL under test. Both paths were converted to the electrical domain and the delay difference between both was measured by a real-time oscilloscope (RTO, Keysight DSA-Z634 A). This procedure was repeated for all 32 SODL settings, while the delay T_0, obtained for the setting '0,' was used to calibrate all the measured values. In Fig. 11(b), the measured and expected delays, and their corresponding deviation, are displayed. For setting '12,' corresponding to a nominal delay of 19.2 ps, the largest deviation was registered, being 0.82 ps.

TABLE I
INSERTION LOSS DECOMPOSITION OF THE PROPOSED OBFN WITH 5-BIT SODLS

Component	Short	Long
Grating coupler	6 dB	
1-to-4 splitter	6.2 dB	
Switch	0.5 dB	
b_a	0.26 dB* + 0.11 dB†	0.26 dB* + 0.015 dB‡
Switch	0.5 dB	
b_b	0.26 dB + 0.11 dB	0.26 dB + 0.030 dB
Switch	0.5 dB	
b_c	0.26 dB + 0.11 dB	0.26 dB + 0.060 dB
Switch	0.5 dB	
b_d	0.26 dB + 0.11 dB	0.26 dB + 0.120 dB
Switch	0.5 dB	
b_e	0.26 dB + 0.11 dB	0.26 dB + 0.240 dB
Combiner	3.1 dB	
Grating coupler	6 dB	

*Reference spiral waveguide loss:
(760 μm × 1.3 dB/cm) + (18 bends × 0.009 dB/bend) = 0.26 dB.
†Light power tapped for characterization.
‡Transmission loss: (70 μm/ps × 1.6 ps × $2^{(\#\,\text{bit-1})}$) × 1.3 dB/cm.

Finally, the insertion loss of the OBFN is decomposed into its components in Table I, indicating that there are three main contributors. First, the fiber-to-chip coupling, realized by grating couplers, is responsible for a loss of 6 dB at 1550 nm.

Second, the 1-to-4 splitter incurs a loss of 6.2 dB, out of which 6 dB is inherent to the power splitting into four channels in the OBFN. Third, the 5-bit SODL introduces losses between 7.225 dB and 7.59 dB, depending on the delay setting, showing that the overall insertion loss only varies by 0.365 dB. The SODL losses can be attributed to switch losses (0.5 dB per switch), waveguide transmission losses (1.3 dB/cm) and bend losses (0.009 dB per 90° bend), and the output power combiners' loss (3.1 dB). In particular, each reference path section, being 760 μm long and having 18 bends, suffers from a waveguide loss of 0.26 dB, and an excess insertion loss of 0.11 dB per tap, due to the introduction of power taps [see Fig. 2(b)] for monitoring purposes. This is listed under the column 'Short' in Table I. The long path sections have an extra length given by 112 μm × 2^{n-1}, with n=1,2,...,5 representing the bit position. The resulting insertion losses are indicated under the column 'Long' of Table I. Future improvements to further reduce insertion loss are discussed in Section VI.

C. Beamforming

The mmWave-over-Fiber RAU was characterized in terms of beamforming performance in an anechoic chamber with the setup illustrated in Fig. 12. In this setup, a 10-dBm CW 1550-nm optical signal (generated by a Yenista T100S-HP/CL laser source) is modulated (by means of a MZM Fujitsu FTM7937EZ biased at quadrature point) by a downlink radio frequency (RF) signal originating from port 1 of the Keysight N5242A PNA-X VNA and amplified by the power amplifier (PA) of the NSI-MI antenna measurement system. An erbium-doped fiber amplifier (EDFA, Keopsys CEFA-C-WDM-LP) brings the level of the optical modulated signal to 13 dBm. Then, the reported

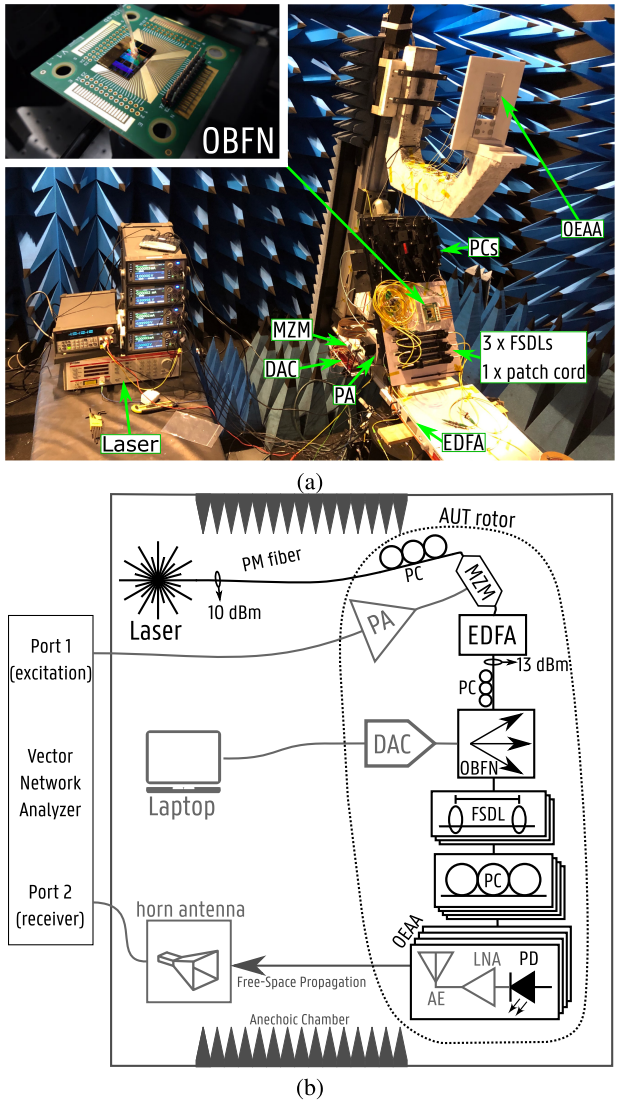

Fig. 12. Setup for measuring the radiation pattern of the optically enabled beamforming RAU, being beamsteered by the OBFN. AE: antenna element; AUT: antenna under test; DAC: digital-to-analog converter; EDFA: erbium-doped fiber amplifier; FSDL: free-space delay line; LNA: low-noise amplifier; MZM: Mach-Zehnder Modulator; OEAA: optically enabled antenna array; PA: power amplifier; PC: polarization controller; PD: photodiode; PM: polarization maintaining.

OBFN splits the modulated optical signal into four channels and adds the required time delays to form a beam towards θ_0. In the setup, optical free-space delay lines (FSDLs, OZ Optics ODL-100-11-1550-9/125-S-60-3A3A-3-1) were used to calibrate out the length differences between the four optical fibers connecting the OBFN to the PDs at the RAU. Additionally, all polarization-dependent components (MZM, OBFN and PDs) are preceded by polarization controllers, manually optimized for maximal optical output power. The signal radiated by the RAU is received by a WR-34 standard gain horn and connected to port 2 of the VNA.

The radiation patterns at 28 GHz obtained by adjusting the OBFN for beam steering to six scan angles from $\theta_0 = 0°$ to $\theta_0 = 51.8°$ are shown in Fig. 13. These radiation patterns are

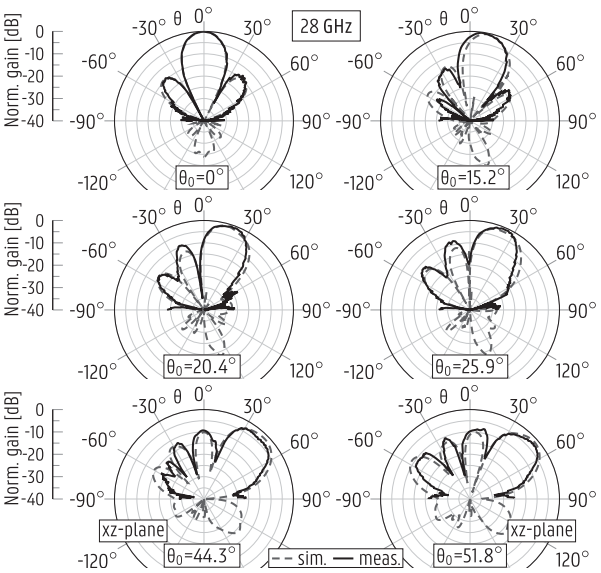

Fig. 13. Measured radiation pattern of the optically enabled beamforming RAU when the OBFN steers the beam to six distinct scan angles (θ_0). All the plots are normalized to the peak gain when beam steering towards $\theta_0 = 0°$.

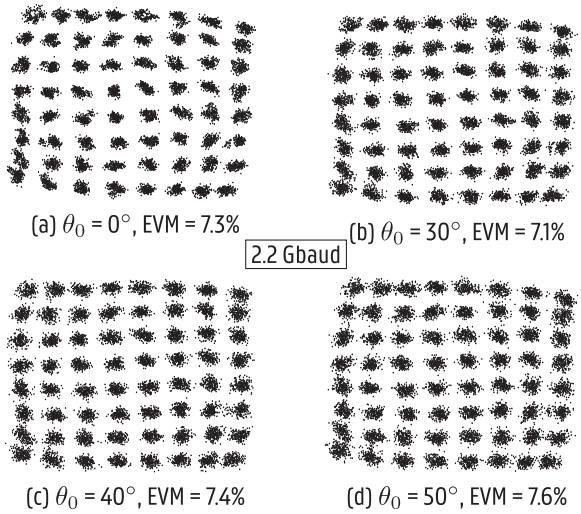

Fig. 14. Measured EVM of a 64 quadrature amplitude modulation (64-QAM) wireless communication link between the proposed RAU and a WG-34 standard gain horn antenna when beam steering to four distinct scan angles.

normalized with respect to the maximum gain at $\theta_0 = 0°$. Good agreement is obtained between simulations and measurements, proving that the gain at the aimed scan angle direction only degrades by at most 0.6 dB and indicating a HPBW of $28° \pm 5°$. Though sidelobe levels up to -5.9 dB are observed, all the displayed radiation patterns are free of grating lobes, which would have levels as high as that of the main beam. Should it be necessary for the application, the side lobe levels could be further reduced by implementing amplitude tapering [29] The beam steering potential of the RAU was also characterized with the proposed OBFN replaced by a 1-to-4 fiber splitter. Then, the optical FSDLs were used to implement the required time delays, obtaining very similar results as in the former experiment. Beam steering towards negative values of θ_0 was not characterized, however they are expected to yield similar results as for the positive θ_0 counterpart, owing to symmetry.

D. Link Performance

The link performance of the RAU was demonstrated by establishing a 13.2-Gbps line-of-sight link to a receiving WG-34 standard gain horn antenna at a distance of 2.35 m and computing the error vector magnitude (EVM) of the received signal when the RAU was adjusted to steer the beam to $\theta_0 =$ 0°, 30°, 40° and 50°. To generate the downlink signal, an arbitrary waveform generator (AWG, Keysight M8195 A) produced a (2^9-1)-bit long pseudo-random binary sequence (PRBS) in a 64 quadrature amplitude modulation (64-QAM) scheme, with a baudrate of 2.2 Gbaud, centered at 28 GHz. Considering the roll-off factor of r = 0.35, this signal completely occupies the 3 GHz available in the n257 5G band. This mmWave signal was injected into an MZM in a similar setup as detailed in Fig. 12, albeit with the OBFN replaced by a 1-to-4 fiber splitter. The PDs of the RAU were biased with a photocurrent of 185 μA and the beamforming delays were inserted by manually adjusting the optical free-space delay lines. The signal received by the horn antenna is amplified by a 25-dB gain LNA (Analog Devices HMC1040), directly connected to the horn antenna output, and recorded by a RTO (Keysight DSA-Z634 A). Next, the EVM is calculated in post-processing, selecting part of the symbol stream as pilot symbols. The resulting detected symbols and their corresponding EVM are shown in Fig. 14. For all steering angles, the EVM remains below the 8% limit for 64-QAM, defined in the 3rd Generation Partnership Project (3GPP) specifications [30]. Remark that even though a single-carrier scheme was used in this experiment, the mmWave-over-Fiber link is modulation agnostic and, thereby, also compatible with orthogonal frequency-division multiplexing (OFDM) [12], adopted in the 5G and WiGig standards. The results demonstrate the excellent performance of the proposed optically enabled RAU and showcases the proposed RAU as an ideal candidate for future use in a large-scale DAS.

VI. State of the Art and Future Work

An overview of state-of-the-art mmWave fiber-wireless experiments is provided in Table II, listing their most important performance metrics, including achieved level of integration between the constituent components, achieved bitrate, RF band, and beam steering capabilities. Table II shows that our mmWave RAU realizes state-of-the-art performance regarding achieved bit rate, level of integration and beam steering performance. While a plethora of optical beamforming implementations have already been proposed [31], [32], only a limited amount of reported mmWave fiber-wireless experiments [8], [11], [12], [33]–[55] effectively demonstrate optical beamforming [40]–[55]. In [44], [45], [47], [54], beam steering is realized by employing bulky external optical delay lines, which are either located at the RAU [44], [45] or at the CO [47]. In addition, various works implement remote beamforming by exploiting

TABLE II
STATE-OF-THE-ART FIBER-WIRELESS LINK EXPERIMENTS

Ref.	Hardware Integration	Bitrate (Gb/s)	Modulation	RF Band (GHz)	Wireless (m)	RoF Type	DL	UL	Beam Steering		
									Type	Location	Range (°)
This	**Array/OEs/AMP**	**13.2**	**64QAM**	**28**	**2.35**	**RFoF**	✓		**OTTD (ext. ODL)**	**RAU**	**-51.8/51.8**
			Carrier	**28**	**2.35**	**RFoF**	✓		**OTDD SOI PIC (SODL)**	**RAU**	**-50/50**
[8]	OE/AMP	24	16QAM	28	2	RFoF	✓	✓	Fixed beam	N/A	N/A
[12]	OE/AMP	8	16QAM	28	3	RFoF	✓				
		12	64QAM	28	1	RFoF	✓				
		7.02	OFDM-16QAM	28	5	RFoF	✓	✓			
		10.53	OFDM-64QAM	28	1	RFoF	✓	✓			
[33]		3.39/0.498	OFDM-64QAM	28	3	IFoF	✓	✓			
		0.87/0.25	OFDM-64QAM	28	3	IFoF	✓	✓			
[34]		4.56	UFOFDM-64QAM	28	0.1	RFoF	✓				
[35]		12	OFDM-16QAM	28	3	RFoF	✓				
[11]		1.37	OFDM-64QAM	28	1.5	SDoF	✓				
[36]		1.5	OFDM-64QAM	28	N/A	IFoF	✓	✓			
[37]		8	SPC-NOMA	60	2.5	RFoF	✓				
[38]		24	16QAM	60	5	IFoF	✓	✓			
		16	16QAM	60	5	IFoF	✓				
		12	QPSK	60	5	IFoF	✓	✓			
[39]		24.08	OFDM-16QAM	60	4	RFoF	✓				
		24.08	OFDM-16QAM	91	3	RFoF	✓				
[42]			Carrier	18-26.5	N/A	RFoF	✓		IPR	N/A	-33.6/33.6
[43]		6	64QAM	28	0.5	IFoF		✓	EPS	RAU	-68/68
[44]		3 × 0.76	OFDM-QPSK	28	5	IFoF/RFoF	✓		OTTD (ext. ODL)	RAU	-30/30
[45]		2.4	OFDM-64QAM	28	5	IFoF/RFoF	✓		OTTD (ext. ODL)	RAU	0/53
[46]	OE/AMP	0.155	32/16QAM (DL/UL)	42.7	1.4	RFoF	✓	✓	OTTD (FD)		-42/42
[47]	Array/UTC-PDs		Carrier	40	0.7	RFoF	✓		Ext. OTTD	CO	-60/60
			Carrier	60	0.3	RFoF	✓		modules	CO	-20/20
		14	16QAM	60	0.5	RFoF	✓		+ VOAs	CO	-30/30
[48]	Array/UTC-PDs	3.5	QPSK	60	0.3	RFoF	✓		OTTD (FD)	CO	
			Carrier	60	0.8	RFoF	✓		OTTD (FD)	CO	0/40
[50]		4 × 1	16QAM	60	1	IFoF	✓		EPS	RAU	-45/45 4 sectors
[51]		1	16QAM	60	1	IFoF		✓	EPS	RAU	-45/45
[52]		10.6† (sum rate)	OFDM-16QAM	60	4	IFoF	✓		EFS	CO	over 8 (sim.)
[53]	LWA/UTC-PD	2.15	OOK	80	0.25	RFoF	✓		EFS	CO	over 22
[54]		10	16QAM	85	0.5	RFoF	✓		Ext. OTTD modules		-35/35
[55]			Carrier	93	0.11	RFoF	✓		OTDD SiN PIC (SODL)		-51/34

Note: Hardware integration is mentioned only for works that focused on it. † Non-standard 15% error vector magnitude criterion for 16QAM. AFSIW = air-filled substrate-integrated-waveguide; CBP = cavity-backed patch antenna; CO = central office; DL = downlink; UL = uplink; DRoF = digital radio-over-fiber; EFS = electronic frequency steering; EPS = electronic phase shifting; FCD = fiber chromatic dispersion; IFoF = intermediate-frequency-over-fiber; IPR = internal path reflection; LWA = leaky wave antenna; NOMA = non-Orthogonal Multiple Access; ODL = optical delay line; OE = opto-electrical transducer; OFDM = orthogonal frequency-division multiplexing; OOK = on-off keying; ORR = optical ring resonator; OTTD = optical true time delay; PM = phase modulator; PS = phase shifter; PIC = photonic integrated circuit; RAU = remote antenna unit; RFoF = radio(/mmWave)-frequency-over-fiber; SDoF = sigma-delta-over-fiber; SiN = silicon nitride; SODL = switchable optical delay line; SOI = silicon on insulator; UFOFDM = universally filtered OFDM; UTC-PD = uni-traveling carrier photodiode.

fiber chromatic dispersion and tunable lasers [46], [48], although thermal stability may limit the usefulness of this approach [56]. Finally, multiple wireless measurement campaigns validate the use of integrated OBFNs, including designs based on optical ring resonators [40], [41], [57], ultra-compact plasmonic phase modulators [49], and SODLs [55]. Furthermore, several mmWave RAUs implementing electrical beamforming [43], [50]–[53] have been proposed. In [50], [51], each dipole AE of the 32-element planar array is connected to a phase shifter and amplifier, enabling high beamforming flexibility at the cost of complexity. The adopted intermediate-frequency-over-fiber (IFoF) architecture requires local oscillator (LO) distribution to each RAU and burdens the RAU with frequency translation, thereby increasing its cost and power consumption. In contrast, [52], [53] propose highly simplified RAU implementations by leveraging the beam steering properties of leaky-wave antennas (LWAs) [58]. Yet, this technique significantly limits beam steering flexibility and frequency reuse. Finally, as indicated by Table II, only a limited number of works [8], [12], [40], [46]–[48], [53] consider the integration of opto-electrical transducers, antenna array and beamforming network in a compact RAU with optimized power-efficiency and beam steering performance. [8], [12] and [46] integrate the opto-electrical transducers and the according amplifiers and drivers in a single compact device, whereas other works focus on integrating uni-traveling carrier photodiodes (UTC-PDs) with a LWA [53] or with the array AEs [47], [48]. This work further increases integration by including a dedicated photodiode and amplifier chain on each highly efficient and compact AFSIW-based AE and by analyzing the potential of a co-design strategy. Interestingly, the AEs in [47], [48] adopt an AFSIW-like cavity-backed patch antenna topology. However, due to their large footprint, the AEs require a substantially larger array inter-element distance (0.75λ at $60\,\mathrm{GHz}$) as compared to this work, limiting the array's grating-lobe-free steering range to only $[-19.5°, 19.5°]$.

Although Table II demonstrates the high performance of the proposed optically-enabled RAU and photonic-integrated beamforming network, there is still room for improvement. First, the performance of the system in terms of range and spectral efficiency is currently noise limited; therefore, the insertion loss of the OBFN should be significantly lowered in future realizations by incorporating two modifications. By replacing the grating couplers by edge couplers [59] and adopting an extra switch at the SODL output instead of the 3-dB combiner,

the insertion loss can be improved by circa 10.5 dB. Second, transfer printing semiconductor optical amplifiers (SOAs) at each OBFN channel [60] will help counteracting the inherent splitting loss and will become essential for large antenna arrays to ensure sufficient light power at each PD. Third, monitor photodiodes should be included in future implementations of the OBFN to determine the switch voltages in real time and to make the circuit more robust to temperature or wavelength variations. By providing a loopback [61] to the central office, the monitor PDs also facilitate antenna system calibration, ensuring optimal performance of the RAUs as well as the tight time/phase synchronization among them when combined with over-the-air (OTA) calibration techniques [62]. Adding these monitor PDs can be done by migrating the design to imec's full Si-Photonics platform iSiPP50G that includes passive and active components, or by making use of transfer printing to print the PDs on top of the grating couplers currently used for calibration of the circuit [63]. This would also enable direct integration of the four PDs of the currently adopted photoreceivers on the OBFN, paving the way for compact integration of the OBFN on the RAU. This does not only mitigate the losses associated with fiber-to-chip coupling, but also eliminates the time-consuming step of gluing the fiber array to the optically enabled antenna array (Section IV-C). In addition, it also guarantees equal optical path lengths for all channels, eliminating the need for the free-space optical delay lines in between the OBFN and the optically-enabled antenna array. Furthermore, in future generations of the OBFN, uplink beamforming should be incorporated to enable bi-directional communication between the UE and RAUs, while Power-over-Fiber techniques should be leveraged to enable remote powering of each RAU. Moreover, the RAU functionality can be further extended to support multiple beams. Each RAU could then serve multiple UEs with simultaneous beams pointed at different directions, occupying the same time and frequency resources, further increasing throughput and spectral efficiency. Last, but not least, to further increase reliability in a large-scale mmWave DAS, dedicated broadband dual-polarized antenna elements should be developed. The aforementioned improvements will turn the RAU into mass-deployable hardware for beamforming DASs.

VII. Conclusion

A low-complexity and efficient remote antenna unit (RAU), featuring broadband wide-angle beam steering, was demonstrated for mmWave-over-fiber distributed antenna systems operating in the [26.5–29.5] GHz 5G N257 band. It consists of a broadband 1×4 uniform linear array (ULA), with four compactly integrated photoreceivers, that is optimized for a grating-lobe-free beam steering range of 100°, and an in-house developed optical beamforming network (OBFN). The ULA's antenna elements (AEs) are implemented in air-filled substrate-integrated-waveguide technology to achieve high antenna efficiency over a broad frequency band, while guaranteeing large isolation between adjacent AEs in compact array configurations. Furthermore, the novel feeding scheme significantly improves the ULA's front-to-back-ratio, thereby enabling compact integration of the photoreceiver modules with minimal interference. It also provides high flexibility for impedance matching the AEs to various loads, enabling co-optimization with the photoreceiver. In particular, we have demonstrated that co-optimization of AE and the photoreceiver's LNA leads to a significantly higher power transfer between both, enabling a broader beam steering range and a total efficiency above 85% for all scan angles between $[-50°, 50°]$. The separately packaged OBFN is implemented on imec's silicon photonics platform. It enables true-time-delay beamforming by means of four switchable optical delay lines that are capable of discretely tuning the delay difference between AEs with a resolution of 1.6 ps up to a maximum delay of 49.6 ps. Through judicious design, an insertion-loss variation of only 0.365 dB along its settings is achieved. Measurements of the stand-alone AEs showed a stable peak gain of 6.8 ± 0.72 dBi, a half-power beamwidth (HPBW) of at least 95° and an inter-antenna isolation of at least 15 dB (mutual coupling <-15 dB) in the operating band. Optical beam steering was demonstrated by steering the RAU's beam up to 51.8° by leveraging the proposed PIC OBFN and comparing the performance to the case where the proposed OBFN is replaced by a 1-to-4 fiber splitter and optical free-space delay lines. In both cases, a good agreement is obtained between the measurements and the simulations, indicating a HPBW of $28° \pm 5°$ and a maximum gain degradation of only 0.6 dB. Furthermore, fiber-wireless experiments demonstrated that the proposed optically enabled ULA successfully establishes a 64-QAM wireless communication link at 2.2 Gbaud (occupying 2.97 GHz and yielding a 13.2 Gbps throughput) while beam steering to four different directions with an EVM below 7.6%. Finally, an in-depth comparison with the state of the art was carried out and future research paths were discussed to further boost the RAU's performance and manufacturability, paving the way for the large-scale roll out of mmWave-over-Fiber-based distributed antenna systems in future generation radio access networks and large intelligent surfaces.

References

[1] M. Matthaiou, O. Yurduseven, H. Q. Ngo, D. Morales-Jimenez, S. L. Cotton, and V. F. Fusco, "The road to 6G: Ten physical layer challenges for communications engineers," *IEEE Commun. Mag.*, vol. 59, no. 1, pp. 64–69, Jan. 2021.

[2] M. Giordani, M. Polese, M. Mezzavilla, S. Rangan, and M. Zorzi, "Toward 6G networks: Use cases and technologies," *IEEE Commun. Mag.*, vol. 58, no. 3, pp. 55–61, Mar. 2020.

[3] M. Shafi et al., "Microwave vs. millimeter-wave propagation channels: Key differences and impact on 5G cellular systems," *IEEE Commun. Mag.*, vol. 56, no. 12, pp. 14–20, Dec. 2018.

[4] X. Song, T. Kühne, and G. Caire, "Fully-/Partially-connected hybrid beamforming architectures for mmWave MU-MIMO," *IEEE Trans. Wireless Commun.*, vol. 19, no. 3, pp. 1754–1769, Mar. 2020.

[5] S. Hu, F. Rusek, and O. Edfors, "Beyond massive MIMO: The potential of data transmission with large intelligent surfaces," *IEEE Trans. Signal Process.*, vol. 66, no. 10, pp. 2746–2758, May 2018.

[6] Q. Wu and R. Zhang, "Towards smart and reconfigurable environment: Intelligent reflecting surface aided wireless network," *IEEE Commun. Mag.*, vol. 58, no. 1, pp. 106–112, Jan. 2020.

[7] M. Di Renzo et al., "Smart radio environments empowered by reconfigurable intelligent surfaces: How it works, state of research, and the road ahead," *IEEE J. Sel. Areas Commun.*, vol. 38, no. 11, pp. 2450–2525, Nov. 2020.

[8] A. Moerman et al., "Beyond 5G without obstacles: MmWave-over-Fiber distributed antenna systems," *IEEE Commun. Mag.*, vol. 60, no. 1, pp. 27–33, Jan. 2022.

[9] A. Moerman et al., "mmWave-Over-Fiber distributed antenna systems for reliable multi-Gbps wireless communication," in *Proc. 3rd URSI Atlantic Radio Sci. Meeting*, 2022, pp. 1–3.

[10] C.-L. I, H. Li, J. Korhonen, J. Huang, and L. Han, "RAN revolution with NGFI (xHaul) for 5G," *J. Lightw. Technol.*, vol. 36, no. 2, pp. 541–550, Jan. 2018.

[11] C.-Y. Wu et al., "Distributed antenna system using sigma-delta intermediate-frequency-over-fiber for frequency bands above 24 GHz," *J. Lightw. Technol.*, vol. 38, no. 10, pp. 2765–2773, May 2020.

[12] L. Bogaert et al., "SiPhotonics/GaAs 28-GHz transceiver with reflective EAM for laser-less mmWave-over-fiber," *J. Lightw. Technol.*, vol. 39, no. 3, pp. 779–786, Feb. 2021.

[13] R. A. Minasian, "Photonic signal processing of microwave signals," *IEEE Trans. Microw. Theory Techn.*, vol. 54, no. 2, pp. 832–846, Feb. 2006.

[14] M. Longbrake, "True time-delay beamsteering for radar," in *Proc. IEEE Nat. Aerosp. Electron. Conf.*, 2012, pp. 246–249.

[15] L. Bogaert et al., "A 5-bit, 1.6 ps resolution true time delay optical beamforming network for 4-element antenna arrays," in *Proc. Int. Topical Meeting Microw. Photon.*, 2021, pp. 1–4.

[16] P. Zheng et al., "A seven bit silicon optical true time delay line for Ka-band phased array antenna," *IEEE Photon. J.*, vol. 11, no. 4, Aug. 2019, Art. no. 5501809.

[17] C. Zhu et al., "Silicon integrated microwave photonic beamformer," *Optica*, vol. 7, no. 9, pp. 1162–1170, Sep. 2020.

[18] Z. Iqbal and M. Pour, "Grating lobe mitigation in wide and near horizon scanning linear arrays with one-wavelength element spacing," in *Proc. IEEE 19th Int. Symp. Antenna Technol. Appl. Electromagn.*, 2021, pp. 1–2.

[19] R. C. Johnson, *Antenna Engineering Handbook*. New York, NY, USA: McGraw-Hill Professional, 1992.

[20] I. L. de Paula et al., "Cost-effective high-performance air-filled SIW antenna array for the global 5G 26 GHz and 28 GHz bands," *IEEE Antennas Wireless Propag. Lett.*, vol. 20, no. 2, pp. 194–198, Feb. 2021.

[21] Q. Van den Brande, S. Lemey, H. Rogier, and J. Vanfleteren, "Coupled half-mode cavity-backed slot antenna for IR-UWB in air-filled SIW technology," in *Proc. IEEE Int. Symp. Antennas Propag. USNC/URSI Nat. Radio Sci. Meeting*, 2018, pp. 1269–1270.

[22] Q. Van den Brande et al., "A hybrid integration strategy for compact, broadband and highly efficient millimeter-wave on-chip antennas," *IEEE Antennas Wireless Propag. Lett.*, vol. 18, no. 11, pp. 2424–2428, Nov. 2019.

[23] R. Kazemi, A. E. Fathy, S. Yang, and R. A. Sadeghzadeh, "Development of an ultra wide band GCPW to SIW transition," in *Proc. IEEE Radio Wireless Symp.*, 2012, pp. 171–174.

[24] L. Bogaert et al., "36 Gb/s narrowband photoreceiver for mmWave analog radio-over-fiber," *J. Lightw. Technol.*, vol. 38, no. 12, pp. 3289–3295, Jun. 2020.

[25] D. M. Pozar, "The active element pattern," *IEEE Trans. Antennas Propag.*, vol. 42, no. 8, pp. 1176–1178, Aug. 1994.

[26] O. Caytan et al., "Compact and wideband transmit opto-antenna for radio frequency over fiber," *Opt. Exp.*, vol. 27, no. 6, pp. 8395–8413, Mar. 2019.

[27] S. Lemey et al., "Air-filled substrate-integrated waveguide technology for broadband and highly-efficient photonic-enabled antenna systems," in *Proc. IEEE XXXIIIrd Gen. Assem. Sci. Symp. Int. Union Radio Sci.*, 2020, pp. 1–4.

[28] Eurocircuits. Accessed: Jul. 4, 2022. [Online]. Available: https://www.eurocircuits.com/

[29] B. Strait, "Antenna arrays with partially tapered amplitudes," *IEEE Trans. Antennas Propag.*, vol. 15, no. 5, pp. 611–617, Sep. 1967.

[30] *3rd Generation Partnership Project; Technical Specification Group Radio Access Network; Evolved Universal Terrestrial Radio Access (E-UTRA); Base Station (BS) Radio Transmission and Reception (Release 17)*, 3rd Generation Partnership Project (3GPP) Std. TS 36.104, Rev. 17.4.0, Dec. 2021.

[31] D. Milovančev, N. Vokić, D. Löschenbrand, T. Zemen, and B. Schrenk, "Analog coherent-optical mobile fronthaul with integrated photonic beamforming," *IEEE J. Sel. Areas Commun.*, vol. 39, no. 9, pp. 2827–2837, Sep. 2021.

[32] S. Pan, X. Ye, Y. Zhang, and F. Zhang, "Microwave photonic array radars," *IEEE J. Microw.*, vol. 1, no. 1, pp. 176–190, Jan. 2021.

[33] J. Kim et al., "MIMO-Supporting radio-over-fiber system and its application in mmWave-Based indoor 5G mobile network," *J. Lightw. Technol.*, vol. 38, no. 1, pp. 101–111, Jan. 2020.

[34] E. Martin et al., "28 GHz 5G radio over fibre using UF-OFDM with optical heterodyning," in *Proc. Int. Topical Meeting Microw. Photon.*, 2017 pp. 1–4.

[35] H.-Y. Wang, Y.-C. Chi, Y.-W. Chen, and G.-R. Lin, "Tri-color optical transmitter with embedding 28-GHz millimeter-wave carrier for 5G mobile over fiber," in *Proc. Conf. Lasers Electro- Opt.*, 2017, pp. 1–2.

[36] M. Sung, S.-H. Cho, J. Kim, J. K. Lee, J. H. Lee, and H. S. Chung, "Demonstration of IFoF-Based mobile fronthaul in 5G prototype with 28-GHz millimeter wave," *J. Lightw. Technol.*, vol. 36, no. 2, pp. 601–609, Jan. 2018.

[37] Y. Tian, K.-L. Lee, C. Lim, and A. Nirmalathas, "Demonstration of non-orthogonal multiple access scheme using multilevel coding without successive interference cancellation with 60 GHz radio-over-fiber fronthaul," in *Proc. Opt. Fiber Commun. Conf. Expo.*, 2018, pp. 1–3.

[38] N. Argyris et al., "A 5G mmWave fiber-wireless IFoF analog mobile fronthaul link with up to 24-Gb/s multiband wireless capacity," *J. Lightw. Technol.*, vol. 37, no. 12, pp. 2883–2891, Jun. 2019.

[39] X. Li et al., "Real-time demonstration of over 20 Gbps V- and W-band wireless transmission capacity in one OFDM-RoF system," in *Proc. Opt. Fiber Commun. Conf. Exhib.*, 2017, pp. 1–3.

[40] C. Tsokos et al., "True time delay optical beamforming network based on hybrid inp-silicon nitride integration," *J. Lightw. Technol.*, vol. 39, no. 18, pp. 5845–5854, Sep. 2021.

[41] M. Morant, A. Trinidad, E. Tangdiongga, T. Koonen, and R. Llórente, "5G NR multi-beam steering employing a photonic TTD chip assisted by multi-core fiber," in *Proc. Opt. Fiber Commun. Conf. Exhib.*, 2019, pp. 1–3.

[42] Y. Chen and R. T. Chen, "A fully packaged true time delay module for a K-band phased array antenna system demonstration," *IEEE Photon. Technol. Lett.*, vol. 14, no. 8, pp. 1175–1177, Aug. 2002.

[43] M.-Y. Huang, Y.-W. Chen, P.-C. Peng, H. Wang, and G.-K. Chang, "A full field-of-view self-steering beamformer for 5G mm-Wave fiber-wireless mobile fronthaul," *J. Lightw. Technol.*, vol. 38, no. 6, pp. 1221–1229, Mar. 2020.

[44] H.-Y. Kao, S. Ishimura, K. Tanaka, K. Nishimura, and R. Inohara, "Spatial multiple beam-steering transmission for 5G multi-user MIMO fiber-wireless systems," in *Proc. Int. Topical Meeting Microw. Photon.*, 2020, pp. 152–155.

[45] H.-Y. Kao, S. Ishimura, K. Tanaka, K. Nishimura, and R. Inohara, "Photodiode-integrated array-antenna module enabling 2-D beamforming for RoF transmission," in *Proc. Opto- Electron. Commun. Conf.*, 2020, pp. 1–3.

[46] M. A. Piqueras et al., "Optically beamformed beam-switched adaptive antennas for fixed and mobile broad-band wireless access networks," *IEEE Trans. Microw. Theory Techn.*, vol. 54, no. 2, pp. 887–899, Feb. 2006.

[47] T. Nagayama, S. Akiba, T. Tomura, and J. Hirokawa, "Photonics-based millimeter-wave band remote beamforming of array-antenna integrated with photodiode using variable optical delay line and attenuator," *J. Lightw. Technol.*, vol. 36, no. 19, pp. 4416–4422, Oct. 2018.

[48] K. Furuya, T. Hirasawa, M. Oishi, S. Akiba, J. Hirokawa, and M. Ando, "60 GHz-Band photonic-integrated array-antenna and module for radio-over-fiber-based beam forming," *IEICE Trans. Commun.*, vol. E100.B, no. 10, pp. 1717–1725, 2017.

[49] R. Bonjour et al., "Plasmonic phased array feeder enabling ultra-fast beam steering at millimeter waves," *Opt. Exp.*, vol. 24, no. 22, pp. 25608–25618, Oct. 2016.

[50] E. Ruggeri et al., "A 5G fiber wireless 4 Gb/s WDM fronthaul for flexible 360° coverage in V-band massive MIMO small cells," *J. Lightw. Technol.*, vol. 39, no. 4, pp. 1081–1088, Feb. 2021.

[51] C. Vagionas et al., "Linearity measurements on a 5G mmWave fiber wireless IFoF fronthaul link with analog RF beamforming and 120° degrees steering," *IEEE Commun. Lett.*, vol. 24, no. 12, pp. 2839–2843, Dec. 2020.

[52] U. Habib, M. Steeg, A. Stöhr, and N. J. Gomes, "Single radio-over-fiber link and RF chain-based 60 GHz multi-beam transmission," *J. Lightw. Technol.*, vol. 37, no. 9, pp. 1974–1980, May 2019.

[53] Á. J. Pascual-Gracia et al., "A photonically-excited leaky-wave antenna array at E-band for 1-D beam steering," *Appl. Sci.*, vol. 10, no. 10, 2020, Art. no. 3474.

[54] T. P. McKenna, J. A. Nanzer, and T. R. Clark, "Photonic beamsteering of a millimeter-wave array with 10-Gb/s data transmission," *IEEE Photon. Technol. Lett.*, vol. 26, no. 14, pp. 1407–1410, Jul. 2014.

[55] Y. Liu, B. Isaac, J. Kalkavage, E. Adles, T. Clark, and J. Klamkin, "93-GHz signal beam steering with true time delayed integrated optical beamforming network," in *Proc. Opt. Fiber Commun. Conf. Exhib.*, 2019, pp. 1–3.

[56] M. Y. Frankel and R. D. Esman, "True time-delay fiber-optic control of an ultrawideband array transmitter/receiver with multibeam capability," *IEEE Trans. Microw. Theory Techn.*, vol. 43, no. 9, pp. 2387–2394, Sep. 1995.
[57] A. B. Smolders et al., "Building 5G millimeter-wave wireless infrastructure: Wide-scan focal-plane arrays with broadband optical beamforming," *IEEE Antennas Propag. Mag.*, vol. 61, no. 2, pp. 53–62, Apr. 2019.
[58] K. Y. Kapusuz, A. V. Berghe, S. Lemey, and H. Rogier, "Partially filled half-mode substrate integrated waveguide leaky-wave antenna for 24 GHz automotive radar," *IEEE Antennas Wireless Propag. Lett.*, vol. 20, no. 1, pp. 33–37, Jan. 2021.
[59] X. Mu, S. Wu, L. Cheng, and H. Y. Fu, "Edge couplers in silicon photonic integrated circuits: A review," *Appl. Sci.*, vol. 10, no. 4, 2020, Art. no. 1538.
[60] B. Haq et al., "Micro-transfer-printed III-V-on-Silicon C-band semiconductor optical amplifiers," *Laser Photon. Rev.*, vol. 14, no. 7, 2020, Art. no. 1900364.
[61] Y. Aoki et al., "Inter-stream loopback calibration for 5G phased-array systems," in *Proc. IEEE Radio Freq. Integr. Circuits Symp.*, 2020, pp. 359–362.
[62] T. Moon, J. Gaun, and H. Hassanieh, "Know your channel first, then calibrate your mmWave phased array," *IEEE Des. Test*, vol. 37, no. 4, pp. 42–51, Aug. 2020.
[63] G. Muliuk et al., "4 × 25 Gbps polarization diversity silicon photonics receiver with transfer printed III-V photodiodes," *IEEE Photon. Technol. Lett.*, vol. 31, no. 4, pp. 287–290, Feb. 2019.

Igor Lima de Paula received the B.Sc. degree in electrical engineering from the Federal University of Juiz de Fora, Juiz de Fora, Brazil, in 2015, and the M.Sc. degree in electrical engineering from Ghent University, Ghent, Belgium, in 2018. Since 2018, he has been a Ph.D. Researcher with IDLab-Electromagnetics Group, Department of Information Technology, Ghent University/IMEC. His research interests include antenna integration in the context of the Internet of Things and the design of multi-antenna systems equipped with microwave photonic devices for radio-over-fiber applications in future mobile communication networks.

Laurens Bogaert received the M.Sc. degree in electrical engineering from Ghent University, Ghent, Belgium, in 2015, and the Ph.D. degree in electrical engineering from the Department of Information Technology, Ghent University—IMEC, Ghent, Belgium, in 2020. Since 2020, he has been a Postdoctoral Researcher with Photonics Research Group, INTEC, Ghent University—IMEC. His current research interests include III/V-on-silicon transfer printing and opto-electronic co-integration for radio-over-fiber links.

Olivier Caytan (Member, IEEE) received the M.Sc. and Ph.D. degrees in electrical engineering from Ghent University, Ghent, Belgium, in 2014 and 2019, respectively. He is currently a Postdoctoral Researcher with Electromagnetics Group, Department of Information Technology, Ghent University/IMEC. His research interests include microwave engineering and active antenna systems, in particular mm-wave opto-electronic antenna systems for 5G and beyond.

Joris Van Kerrebrouck was born in Ghent, Belgium, in 1989. He received the M.S. degree in electronics engineering from Ghent University, Ghent, Belgium, in 2014, and the Ph.D. degree from Intec Design Group. In 2014, he joined the Intec Design Group. His current interests include high-speed SiGe BiCMOS analog circuits and systems for high-speed optical-electrical transceivers.

Arno Moerman (Graduate Student Member, IEEE) received the M.Sc. degree from Ghent University, Ghent, Belgium, in 2019. He is currently a Ph.D. Researcher with the Department of Information Technology, Ghent University/IMEC, Ghent, Belgium. His research focuses on antenna systems for future generation mobile communication networks.

Muhammad Muneeb was born in 1982, in Pakistan. He received the B.S. degree in electronic engineering from the GIK Institute of Engineering and Technology, Swabi, Pakistan, in 2005, and the Erasmus Mundus Masters degree in photonics from the Royal Institute of Technology, Stockholm, Sweden, and the University of Ghent (UGent), Ghent, Belgium, in 2010. Since November 2010, he has been with Photonics Research Group, INTEC, UGent, where his research focuses on III–V/Si photonic circuits for MidIR spectroscopic applications.

Quinten Van den Brande was born in Ghent, Belgium, in 1991. He received the M.Sc. degree in electronics engineering from Campus Schoonmeersen, Ghent University, Ghent, Belgium, in 2016, and the Ph.D. degree in electrical engineering from Ghent University, in 2021. His research interests include ultra-wideband localization systems and fully integrated next-generation (5G and beyond) communication systems-on-chip.

Guy Torfs (Senior Member, IEEE) received the Engineering degree in applied electronics and the Ph.D. degree in applied sciences and electronics from Ghent University, Ghent, Belgium, in 2007 and 2012, respectively. Since 2011, he has been with IMEC, Ghent University, where he first became a part-time Assistant Professor in 2015. In 2018, he became full-time Associate Professor with Ghent University. His research interests include high-speed mixed-signal designs for wireless, fiber-optic and backplane communication systems, including digital signal processing and calibration, analog equalization circuits, radio-over-fiber transceivers, and clock and data recovery systems. In 2014, as part of the Bi-PON and Cascaded Bi-PON team, he was the recipient of the Greentouch 1000x Award. He was a co-recipient of a 2015 DesignCon Best Paper Award in the high-speed signal design category and 2019 ECOC Best Demo Award.

Johan Bauwelinck (Senior Member, IEEE) was born in Sint-Niklaas, Belgium, in 1977. He received the M.Sc. degree and the Ph.D. degree in electrical engineering from Ghent University, Ghent, Belgium, in 2000 and 2005, respectively. Since October 2009, he has been a Professor with IDLab Research Group, Department of Information Technology (INTEC), Ghent University, and IMEC, where he has been leading the Design Lab since 2014 (currently 30 people strong). His research focuses on high-speed, high-frequency (opto-)electronic circuits and systems, and their applications on-chip and board level, including transmitter and receiver analog front-ends for fiber-optic communication or instrumentation systems. He was and is very active in EU-funded projects in FP6, FP7, and Horizon 2020, such as Optima, Streams, HandheldOCT, POETICS, and ESA protobix conducting research on advanced electronic integrated circuits for next generation optical networks, photonic satellite payloads and integrated optical sensing. He has promoted 27 Ph.D.s and coauthored more than 350 publications and ten patents in the field of high-speed electronics and fiber-optic communication. In 2020, he cochaired the Technical Program Committee of the European Conference on Optical Communications (ECOC) and in 2022, he became an Associate Editor of the IEEE TRANSACTIONS ON CIRCUITS AND SYSTEMS II: EXPRESS BRIEFS.

Hendrik Rogier (Senior Member, IEEE) received the M.Sc. and Ph.D. degrees in electrical engineering from Ghent University, Ghent, Belgium, in 1994 and 1999, respectively. From 2003 to 2004, he was a Visiting Scientist with Mobile Communications Group, Vienna University of Technology, Vienna, Austria. He is currently a Senior Full Professor with the Department of Information Technology, Ghent University, and a Guest Professor with Interuniversity Microelectronics Centre, Ghent. He has authored or coauthored more than 195 papers in international journals and more than 215 contributions in conference proceedings. His current research interests include antenna systems, radio wave propagation, body-centric communication, numerical electromagnetics, electromagnetic compatibility, and power/signal integrity. He is a member of the MTT-26 RFID, Wireless Sensor, and IoT Committee, and he is the URSI Commission B representative for Belgium. He was the recipient of the URSI Young Scientist Award (twice) at the 2001 URSI Symposium on Electromagnetic Theory and at the 2002 URSI General Assembly, 2014 Premium Award for Best Paper in the *IET Electronics Letters*, Best Paper Award First Place in the 2016 IEEE MTT-S Topical Conference on Wireless Sensors and Sensor Networks, Best Poster Paper Award at the 2012 IEEE Electrical Design of Advanced Packaging and Systems Symposium, Best Paper Award at the 2013 IEEE Workshop on Signal and Power Integrity, and Joseph Morrissey Memorial Award for the First Best Scientific Paper at BioEM 2013. From 2017 to 2019, he was an Associate Editor for IEEE TRANSACTIONS ON MICROWAVE THEORY AND TECHNIQUES. He is currently an Associate Editor for *IET Electronics Letters* and of *IET Microwaves, Antennas and Propagation*.

Piet Demeester (Fellow, IEEE) is currently a Professor with Ghent University (UGent), and the Director of IDLab, IMEC Research Group, UGent. At IDLab his research interests include distributed intelligence in IoT, machine-learning and datamining, semantic intelligence, cloud and Big Data infrastructures, fixed and wireless networking, electromagnetics, and high-frequency circuit design. He is a holder of an advanced ERC grant.

Günther Roelkens (Senior Member, IEEE) received the degree in electrical engineering from Ghent University, Ghent, Belgium, in 2002, and the Ph.D. from the Department of Information Technology, Ghent University, in 2007. He is currently a full Professor with the Department of Information Technology (INTEC), Ghent University. In 2008, he was a Visiting Scientist with IBM TJ Watson Research Center, New York, NY, USA. His research interests include heterogeneous integration of III-V semiconductors and other materials on top of silicon waveguide circuits and electronic/photonic co-integration. He was holder of an ERC starting grant (MIRACLE), to start up research in the field of integrated mid-infrared photonic integrated circuits.

Sam Lemey (Member, IEEE) received the M.Sc. degree in electronic engineering from Howest, University College West Flanders, Kortrijk, Belgium, in 2012, and the Ph.D. degree in electrical engineering from Ghent University, Ghent, Belgium, in 2016. He is currently a Professor with the Department of Information Technology (INTEC), Ghent University/IMEC. From January to March 2018, he was a Visiting Scientist with Terahertz Photonics Group, Institute of Electronics, Microelectronics and Nanotechnology (IEMN), University Lille Nord de France, Lille, France. His research interests include antenna systems for wearable applications, active antenna design for the Internet of Things and (beyond) 5G applications, (opto-electronic) millimeter-wave multi-antenna systems, impulse-radio ultra-wideband antenna systems for centimeter-precision localization, and full-wave/circuit co-optimization frameworks to realize (opto-electronic) active (multi-)antenna systems. He was the recipient of the URSI Young Scientist Award at the 2020 URSI General Assembly and was awarded the Best Paper Award at the 2016 IEEE MTT-S Topical Conference on Wireless Sensors and Sensor Networks. He was also a co-recipient of the 2015 Best Paper Award at the 22nd IEEE Symposium on Communications and Vehicular Technology in the Benelux and 2019 ECOC Best Demo Award.